RESEARCH

The Role of TiO$_2$ on ZnAl$_2$O$_4$ Spinel Prepared by Direct Coagulation Casting Method: Physico-mechanical, Optical, Structural and Antimicrobial Properties

H. E. H. Sadek[1] · A. E. Reda[1] · R. M. Khattab[1] · M. A. Hessien[1]

Abstract

This work represents the shaping of alumina–zinc oxide (AZ) samples with the direct coagulation casting method. The effect of zinc oxide (0, 10, 20, 30, and 40 wt%) and the firing temperatures on the phase composition, microstructure, physical properties, and mechanical properties of the AZ samples were studied. The effect of titanium oxide (2, 5, and 7 wt%) and the firing temperatures on the phase composition, microstructure, physical properties, and mechanical properties of the AZ sample with 40 wt% of zinc oxide were studied. Furthermore, the optical properties, magnetic properties, and antimicrobial activity were measured. The results indicate that the increase in zinc oxide enhances the formation of zinc aluminate, which has a gahnite phase. Moreover, increasing the zinc oxide increases the apparent porosity and decreases the grain size and bulk density at various firing temperatures. On the other hand, the addition of 5 wt% titanium oxide increases the bulk density to 3.5 g/cm^3 compared to 1.72 g/cm^3 with no titania. The apparent porosity and compressive strength reached 5% and 69.2 MPa after 5 wt% TiO$_2$ addition; respectively, compared to 59% and 27.2 MPa with no titania addition. The prepared samples show promising optical band gap of 2.98–3.97 eV, a mixed magnetic behavior, and favorable antibacterial activity against *E. coli*, *S. aureus*, *B. cereus* strains.

Keywords Direct coagulation casting · Alumina–zinc oxide · Titania · Spinel · Compressive strength

1 Introduction

Gahnite is the mineral form of ZnAl$_2$O$_4$ spinel. Moreover, it is known as a two-cation oxide spinel that has a cubic structure (space group Fd-3m) [1]. The spinel has the general formula of AB$_2$O$_4$ where A is a divalent cation taking tetrahedral positions and B is a trivalent cation occupying octahedral positions. It is known to have diamagnetic properties and a wide band gap (3.8 eV) [2, 3]. It has been reported that adding TiO$_2$ to ZnAl$_2$O$_4$ tunes the crystal size which indeed results in a higher density and a better dielectric permittivity [4, 5]. Furthermore, Xu et al. reported that TiO$_2$ is used as a nucleating agent [6].

Zinc aluminate possesses remarkable traits like low surface acidity, robust mechanical durability, and remarkable chemical and thermal stability [7–9]. Due to these outstanding attributes, these materials have been employed across diverse applications, such as serving as a host matrix, optical coatings in aerospace, and refractory substances. Zinc aluminate has notably played a significant role in various processes, including its extensive use as a photocatalyst in applications like the degradation of organic dyes in wastewater treatment through photocatalysis [9–11]. Furthermore, zinc aluminate has a crucial role as a catalyst support in a range of organic conversions, including the synthesis of heavy alcohols, methanol, and the conversion of saturated alcohols into olefins [9, 12, 13].

Due to its significant importance, various synthesis methods have been employed for zinc aluminate, encompassing co-precipitation, combustion, sol–gel, hydrothermal, microwave-hydrothermal, and solid-state reaction (SSR) techniques, as outlined in references [5, 14–17].

Solid-state reactions (SSR), while advantageous in some aspects, come with drawbacks such as inhomogeneity, limited control over stoichiometry, elevated temperatures, reduced surface area, and occasionally necessitating

✉ A. E. Reda
  aisha_ezz@yahoo.com

1 Refractories, Ceramics, and Building Materials Department, National Research Centre, Dokki, Cairo 12622, Egypt

machinery for product advancement [18]. Nonetheless, SSR offers simplicity in execution, often utilizing readily available, cost-effective starting materials without the need for solvents. Consequently, end products don't demand extensive purification to eliminate solvents and impurities. One of SSR's key merits lies in its high yield, making it economically advantageous compared to alternative synthesis methods [15]. Presently, the prevailing trend focuses on shaping the product through near-net shaping techniques like direct coagulation methods that employ dispersants, binders, and cost-effective molds for part formation. This innovative approach tackles issues of inhomogeneity and enables cost-effective manufacturing.

Shaping porous ceramics can be achieved through machinery-based methods or machinery-free methods. Machinery-based shaping methods include injection molding, hot isostatic pressing and electro spinning. Machinery-free shaping technologies include gel casting, direct coagulation casting (DCC), and temperature-induced forming [19–21]. DCC is based on the preparation of a stable slurry far away from the pH of the zero−point charge (pH_{zpc}) then imitating the coagulation through a pH change close to the pH_{zpc}. The pH change can be induced by an enzymatic or a thermal decomposition. The enzymatic decomposition DCC is performed by using urea-urease in an acidic media or glucose–glucose oxidase in a basic media [22]. Urease is an enzyme that decomposes urea into ammonia and increases the pH. At temperatures below 5 °C, urease is inactive which offers the possibility that the suspension of the metal oxides can be moved to a mold. When coagulation is necessary, the temperature is raised and urea breakdown begins, as illustrated in the equation below (1) [23].

$$CO(NH_2)_2 + 2H_2O \rightarrow 2\,NH_3 + H_2CO_3 (\text{buffer pH}\,9) \quad (1)$$
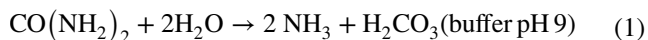
Santos et al. prepared Cu-doped $ZnAl_2O_4$ as an environmentally friendly pigment through a combustion method. Pigments have shown colors between yellow and red [24]. In another publication, they applied the same synthesis method to prepare Ni-doped $ZnAl_2O_4$ with color ranges between blue and green [25]. Belyaev et al. prepared $ZnAl_2O_4$ powders through sol–gel synthesis followed by calcinations at 900 °C. They used the calcined $ZnAl_2O_4$ powder to prepare transparent ceramic by hot isostatic pressing [26]. Siragam et al. prepared zinc aluminate particles $(1 − x) ZnAl_2O_4 − x\,TiO_2$ powder, $x = 0.1$ with a sol–gel method [4, 5]. The DCC method was used to prepare porous $Al_2O_3–TiO_2$ ceramics [27]. Wang et al. prepared $ZnAl_2O_4$ porous ceramic with a pore-forming method. They used PEG as a pore-directing agent and changed the weight% between 10 and 24%. Their results showed that increasing the pore-forming agent resulted

in an increase in the porosity from about 54–63%; on the other hand, the compressive strength decreased from about 16 to 12 MPa [28].

Photocatalysts provide versatile applications in fields as water remediation and energy application. Several metal oxides, natural clays and spinels have been applied as photocatalysts towards organic molecules [29, 30]. Putra has applied $ZnAl_2O_4$ spinel as a photocatalyst for P-nitrophenol under visible light and it took 9 min to change from yellow to colorless [13]. Tangcharoen et al. prepared iron doped zinc aluminate by sol–gel auto-combustion and applied it in the photodegradation of rhodamine B (RhB), methylene blue (MB), methyl orange (MO), and methyl red (MR) with 98% degradation [31]. Pipattanaporn et al. reported that zinc aluminate possesses a broad bandgap that finds applications in luminescent materials and light-emitting diodes as well as photocatalytic and photodegradation processes [32].

In their studies, Foletto et al. observed that $ZnAl_2O_4$ particles exhibited outstanding photocatalytic performance in decomposing Procion Red dye from aqueous solutions [33]. Gahnite, produced through mechano-chemical methods, was investigated for its photocatalytic potential in degrading Chromium Acidic Black dye under UV light exposure [34]. Using a wet chemical solution-phase approach, $ZnAl_2O_4$ nanospheres were synthesized and displayed effective photocatalytic activity in breaking down Rhodamine B dye [35]. Furthermore, when assessed for photocatalytic capability under UV irradiation, $ZnO/ZnAl_2O_4$ microspheres demonstrated significantly enhanced efficiency in the photodegradation of Methylene Blue dye compared to commercial ZnO powder [36].

Current materials production research aims to overcome the limitations associated with Solid-State Reaction (SSR), particularly the challenges of achieving nanoscale size and structural uniformity. One approach to enhance SSR involves the use of direct coagulation casting. Additionally, researchers have successfully synthesized porous gahnite using a pore-directing agent. However, there is a significant research gap when it comes to exploring the application of direct coagulation casting for forming porous gahnite. Furthermore, the study of composite materials comprising porous gahnite and titanium oxide at various concentrations remains unexplored.

The present work reports, for the first time to our knowledge, the effect of the weight ratio of alumina and zinc oxide on the formation of zinc aluminate spinel (AZ) shaped by DCC. Moreover, the effect of TiO_2 on the characteristics of the spinel is studied as well as the effect of the firing temperatures. The prepared samples were characterized by XRD and SEM, and the physical, optical, magnetic, and mechanical properties were measured.

Table 1 The compositions of alumina–zinc oxide ceramic bodies with different ZnO ratios and formed by DCC method

Sample name	Raw materials (wt%)		Batch compositions (g)			
	Al_2O_3	ZnO	Al_2O_3	ZnO	Water	Gelatin
AZ0	100	0	75.86	0	22.14	2
AZ10	90	10	68.27	7.59	22.14	2
AZ20	80	20	60.69	15.17	22.14	2
AZ30	70	30	53.10	22.76	22.14	2
AZ40	60	40	45.52	30.34	22.14	2
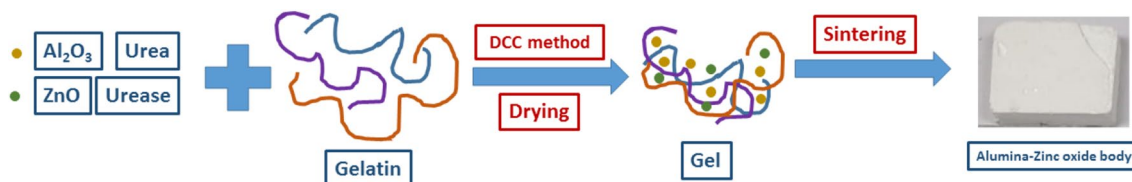
Scheme 1 Schematic drawing of direct coagulation casting method (DCC) to form alumina–zinc oxide bodies

2 Materials and Experimental Methods

2.1 Materials

Urea extra pure 99%, Merck Schuelardt, SDFCL, M.Wt. 60.06 g, CAS NO (57-13-6); urease, alfa Aesar, USA, CAS NO 9002-13-03; sulphuric acid, biochem, ammonium citrate tribasic (ACT) (97%) (Alfa Aesar), 96–98%; calcined alumina, Asfour company (size < 63 μm), titanium oxide anatase (Riedel-de haen), ZnO (Fluka, 99.9%), commercial gelatin, nutrient agar (NA) medium (2 g/L yeast extract, 5 g/L peptone, 1 g/L meat extract, 5 g/L NaCl, and 15 g/L agar, pH 7.4), and nutrient broth medium (2 g/L yeast extract, 5 g/L peptone, 1 g/L meat extract, 5 g/L NaCl, and pH 7.4).

2.2 Experimental Methods

Five alumina samples of varying weight ratios of zinc oxide (0, 10, 20, 30 and 40 wt%) at the expense of alumina in addition to 0.6 wt% ACT based on powder and 0.6 mol/L of urea were used to prepare suspended ceramic slurries according to Table 1. The samples are named AZ0, AZ10, AZ20, AZ30, and AZ40 where the two digits indicate the weight ratio of zinc oxide.

pH 4 acidic slurries were prepared by addition of H_2SO_4. At 5 °C, urease was injected as 1 unit per gram of solid powders [23, 37] followed by gelatin which is used as a binder to improve the sturdy of green bodies. Urease is an enzyme that induces a change in the pH from 4 to 9. Because the urease enzyme is inactive at 5 °C and does not react with the urea substrate, the slurry can be poured into the molds. Air removal was performed for 10 min at 10 mbar at temperatures below 5 °C and used to remove most dissolved air. Then, the suspension temperature is raised to 20–40 °C to activate Urease. The activated urease enzyme reacts with urea which increases the pH and encourages coagulation. In general, a unit of urease enzyme releases 1 mol of ammonia from one mol of urea at 25 °C. The sample was then removed and dried for seven days at 25 °C and 90% relative humidity. The firing temperatures were 1550 °C, 1600 °C, and 1650 °C with a heating rate of 3 °C/min up to 600 °C then the heating rate is 7 °C/min up to the desired firing temperature. Representative scheme for the synthesis method is shown in Scheme 1.

To study the effect of titania on spinel formation, three different compositions were formed. Sample AZ40 was used as an optimum with 2, 5, and 7 wt% TiO_2 at the expense of alumina. The samples named AZ40T2, AZ40T5 and AZ40T7 and their compositions are listed in Table 2.

2.3 Characterization Methods

The zeta potential was measured for seven different compositions at pH 4 which is adjusted with H_2SO_4. The zeta potential of 60 wt% Alumina: 40 wt% zinc oxide was measured under the effect of changing ACT concentration (0.3 wt%, 0.6 wt%, and 0.9 wt% based on powder). Then, the zeta potential was studied under the effect of consecutive addition of urea, urease, and gelatin to 60 wt% Alumina: 40 wt% zinc oxide in the presence of 0.6 wt% ACT. Finally, the change of zeta potential under the effect of adding 5 wt% of TiO_2 was measured. For example, a sample preparation was made from a solid loading of 5 vol% powder. The slurry was left under continuous stirring for 24 h. The slurry was diluted by a ratio of 0.4 mL into 200

Table 2 The compositions of TiO$_2$–ZnAl$_2$O$_4$ spinel ceramic bodies with different TiO$_2$ ratios and formed by DCC method

Sample name	Raw materials (wt%)			Batch compositions (g)				
	Al$_2$O$_3$	ZnO	TiO$_2$	Al$_2$O$_3$	ZnO	TiO$_2$	Water	Gelatin
AZ40T2	58	40	2	44.61	30.34	0.91	22.14	2
AZ40T5	55	40	5	43.24	30.34	2.28	22.14	2
AZ40T7	53	40	7	42.33	30.34	3.19	22.14	2

mL, resulting in a solid load of 0.01% for zeta measurement which was done on Zeta Sizer 2000, Malvern (UK).

To identify the crystalline phases of fired samples at optimal firing temperature, a Bruker D8 Advance Diffractometer with secondary monochromatic beam CuK radiation at 40 Kv and 40 mA was used. Before SEM analysis, samples were coated with just a tiny amount of gold. The microstructure of burnt ceramic bodies was investigated using the Philips XL30 scanning electron microscopy (SEM) model, which has a 30 kV accelerating voltage and a magnification of up to 400000×.

The ASTM-C20 bulk density (BD) and apparent porosity (AP) were determined using the Archimedes method. Based on 2 h of water immersion in a vacuum discator, Archimedes' displacement technique was applied to evaluate the bulk dentistry and apparent porosity. The saturated sample was weighted (Ws) in the air before being immersed in water (Wi). After leaving the sample to dry at hundred °C for 24 h, the dry weight (W$_d$) of the sample was recorded.(γ) is the specific gravity of the water. The samples' bulk density (BD) and apparent porosity (AP) were calculated using formulae (2 and 3); respectively: [38, 39].

$$AP = \frac{Ws - Wd}{Ws - Wi} \times 100 \qquad (2)$$

$$BD = \frac{Wd}{Ws - Wi} \times \gamma \qquad (3)$$

The linear shrinkage of the fired samples was calculated using Eq. (4):

$$Shrinkage(\%) = \frac{L_{green} - L_{sintered}}{L_{green}} \times 100 \qquad (4)$$

where L$_{green}$ is the dimension before sintering and L$_{sintered}$ is the dimension after firing. The hydraulic testing machine, model Seidner, Riedlinger, Germany, with a maximum loading capacity of 600 kN, was used to measure the compressive strength of the burned specimens. The diffuse reflectance UV–Visible spectra were recorded using a Thermo Scientific Evolution 300 UV–Visible spectrophotometer to estimate the optical properties of the fired samples. Magnetic

measurements were conducted using a Lakeshore VSM 7410 model, equipped with a 3 T magnet.

The antimicrobial activity was determined using Well Diffusion Method against Gram negative bacteria [*Escherichia coli*, (ATCC25922)] and Gram positive bacteria [*Staphylococcus aureus*, (ATCC 6538)] and [*Bacillus cereus*, (ATCC 6629)] according to Chen et al. with minor modification [40]. Moreover, 10 mcg of Gentamicin was used as a standard antibiotic disc. Fresh overnight broth medium was used to generate the pathogenic strains, which then underwent cultivation at 37 °C. This pathogenic strain's inoculums quantity was generated and adjusted to about 0.5 McFarland standard (1.5×10^8 CFU/mL), and a 25.0 µL inoculums size of each microorganism strain was independently injected onto every plate containing 20.0 mL of the sterile nutritional agar medium (NA). Wells were punctured by 1.0 cm cork borer in the inoculated agar plates. About 100.0 µl of each sample (50 mg/mL) was put in one of the wells. The plates were placed in the the refrigerator for 1 hour for more diffusion of these samples. After 24 h of incubation at 37 °C, zones of inhibition (ZI) were determined in millimeter. Exempt from Ethical review; Approval for Exempt Review No.: EX010052023.

3 Results and Discussion

3.1 Zeta Potential of Ceramic Slurries

Figure 1a shows the measured zeta potential of 60 wt% alumina–40 wt% zinc oxide slurries at different dispersant concentrations based on the powder. The metal oxide slurries' zeta potential with 0.3 wt%, 0.6 wt%, and 0.9 wt% of ACT are − 4.3 mV, − 4.98 mV, and − 6.59 mV, respectively. With rising ACT, the zeta potential climbs. The dissociation of ACT in water results in the formation of ions represented in Eq. (5). Negative citrate ions stabilize metal oxides through formation of an electric double layer [41, 42].
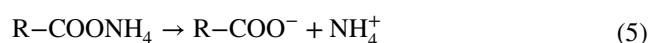
$$R-COONH_4 \rightarrow R-COO^- + NH_4^+ \qquad (5)$$

Figure 1b, the addition of urea to the ceramic slurry with ACT (0.6 wt%) results in the increase of zeta potential to
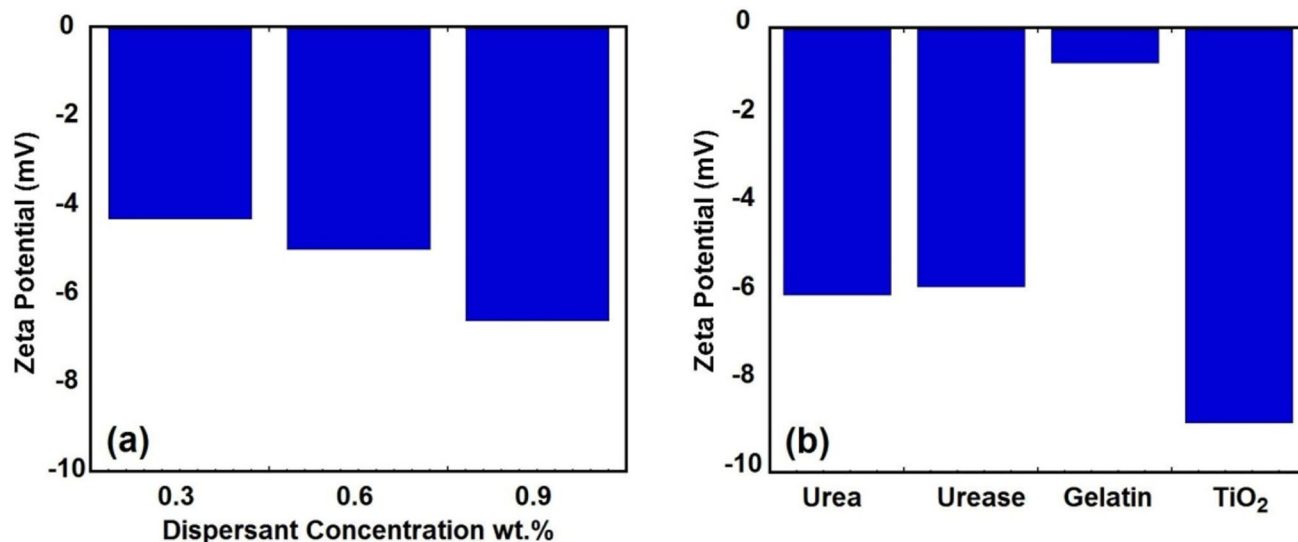
Fig. 1 Zeta Potential of slurries **a** as a function of dispersant concentration and at alumina: zinc oxide wt% = 60:40, **b** as a function of other additives and at dispersant 0.6 wt%

-5.99 mV instead of -4.98 mV for the sample without urea. The further addition of urease to the sample with urea (-5.99 mV) resulted in a slight decrease of zeta potential to -5.81 mV but still the measured zeta potential is better than the sample with 0.6 wt% ACT only (i.e., -4.98 mV). This may be related to the disturbance of double layers. The addition of gelatin resulted in a drastic decrease of zeta potential to -0.76, which could be connected to the agglomeration's formation. However, the addition of 0.5 wt% of titania followed by a high increase in the zeta potential to -8.879 mV. Ceramic particles can be dispersed in stable aqueous colloidal solutions which are attained throughout the production of very charged exteriors, that can be attained by the addition of a dispersant, and further improved by adding TiO_2. In the case of alumina–zinc oxide–titania suspensions with ACT as a dispersing agent, a highly negative potential was achieved -8.879 mV.

3.2 Phase Compositions

Figure 2a represents the XRD diagrams of the ceramic bodies of alumina–zinc oxide prepared by DCC of alumina and zinc oxide in different compositions (Table 1) followed by firing at 1650 °C for 1 h. This temperature is chosen as an optimum according to the physical properties, which will be discussed later. The sample AZ0 that is composed of pure alumina shows peaks at $2\theta = 25.63°$, $35.2°$, $37.8°$, $43.39°$, $52.60°$, $57.72°$ which correspond to (102), (104), (110), (113), (204) and (116) planes of corundum; respectively, according to the card (96-100-0033). Sample AZ10 which has 10 wt% of ZnO and 90 wt% alumina shows the corundum peaks exactly as sample AZ0. Sample AZ20, which
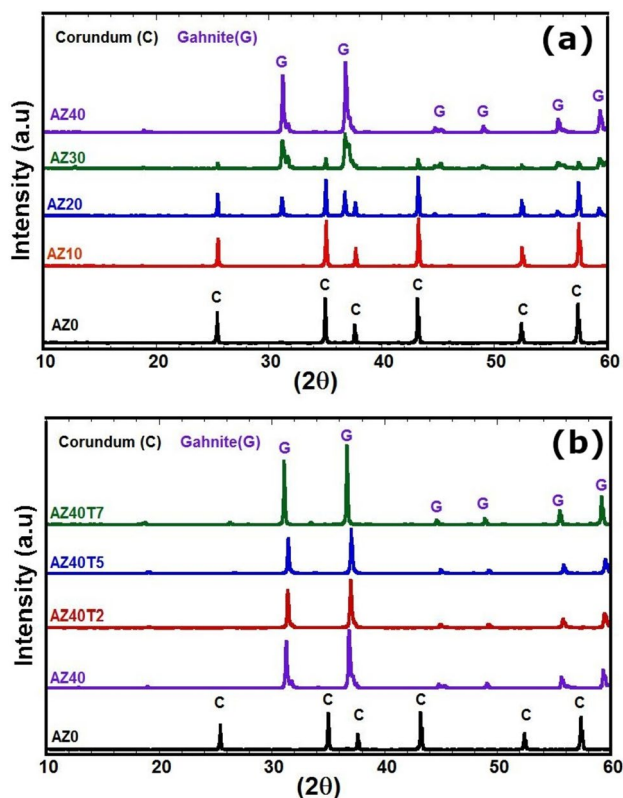

Fig. 2 The XRD diagrams of **a** the fired alumina–zinc oxide (AZ) bodies and **b** the fired TiO_2–zinc aluminate (AZT) bodies

contains 20% by weight of ZnO and 80 wt% alumina shows new peaks at $2\theta = 31.22°$ and $36.80°$ of gahnite and all peaks corresponding to corundum. Sample AZ30 shows an

increase in the intensity of peaks related to gahnite and a decrease in the intensity of peaks related to corundum. Sample AZ40 shows peaks related to gahnite only and no peaks are observed for corundum, and it has been chosen to study the effect of adding different ratios of titania. Gahnite formation is a solid-state reaction between alumina and zinc oxide at elevated temperature and stoichiometric ratio according to the following Eq. (6) [43]:

$$Al_2O_3 + ZnO \rightarrow ZnAl_2O_4 \tag{6}$$

El-Mehalawy et al. reported that the formation of zinc aluminate is achieved through the substitution of Zn^{2+} by Al^{3+} as their size is 0.74 and 0.54; respectively [43].

Figure 2b represents the XRD diagrams of ceramic bodies prepared by DCC of alumina, zinc oxide, and titanium oxide at different compositions (Table 1) followed by firing at 1600 °C for 1 h. This temperature is chosen as an optimum according to the physical properties, which will be discussed later. Samples AZ40T2, AZ40T5 and AZ40T7 show peaks at $2\theta = 31.22°, 36.65°, 44.76°, 49.02°, 55.59°,$ and $59.27°$ which correspond to (202), (311), (400), (313), (422) and (511) planes of gahnite; respectively according to the card (96-901-3643). It seems that adding titanium oxide to the composition of sample AZ40 results in the formation of the gahnite phase at temperature of 1600 °C compared to sample AZ40 fired at 1650 °C.

After the addition of titania, the absence of additional peaks shows that no secondary phases are formed, which indicates that Ti ions are well incorporated with zinc ions without affecting the parent gahnite structure [44]. It is worth mentioning that adding titania results in a peak shift in plan (311). The plan (311) is observed at $2\theta = 36.79°, 37°,$ $37.05°,$ and $36.67°$ for samples AZ40, AZ40T2, AZ40T5, and AZ40T7; respectively. This may be attributed to the displacement of Zn^{2+} (0.74 Å) by smaller size Ti^{4+} (0.68 Å). This displacement can induce a change in the planar distance, which has been reflected in the peak shift [24, 45, 46]. Furthermore, it has been reported that the change to a higher angle may be related to a reduction of the unit cell and better crystallinity [47].

3.3 Microstructure

Figure 3 shows the SEM images of alumina–zinc oxide ceramic bodies with different ZnO ratios and fired at 1650 °C for 1 h. Figure 3a and b represents sample AZ0 which is composed of pure corundum and appears as a hexagonal plated shape. As discussed in the XRD, gahnite was produced after the inclusion of zinc oxide, which has polygonal grains [48]. Generally, two types of pores are identified. Smaller pores exist within the particles and are known as intra-particle pores. These originate from the decomposition

of starting materials. Larger pores, located at the intersections of particles, are referred to as inter-particle pores and result from the packing behavior of mixed powders. In this study, the focus is on intergranular pores and fine neck bonds. The introduction of ZnO leads to an increase in the quantity of intergranular pores.

The increase in ZnO wt%, in samples AZ0, AZ10, AZ20, AZ30, and AZ40, hinders the grain growth and leaves more pores, as seen in Fig. 3b, d, f, g, h, and j; respectively [43]. Hence, the surplus ZnO that remained between the grains served as a barrier, impeding boundary movements, and restricting the growth of the grains [49, 50]. Consequently, this hindered the migration of boundaries, potentially explaining the decrease in density as discussed further in Sect. 3.4.

Figure 4 shows the SEM images of $ZnAl_2O_4$ spinel ceramic bodies with different TiO_2 ratios. It can be seen from comparing SEM images of sample AZ40 (Fig. 3j) with SEM images of sample AZ40T2 (Fig. 4b) that adding titania results in an increase in the grain size which results in a decrease in the porosity. Interparticle pores exhibit a notable reduction in size, accompanied by coarser neck bonds when TiO_2 is introduced at concentrations of up to 5 wt%. However, beyond this threshold of 5 wt% TiO_2 addition, there is a noticeable increase in interparticle pores [49]. The same trend is seen when comparing Fig. 4b and d as titania content is increased from 2 to 5 wt% in samples AZ40T2 and AZ40T5. Figure 4c and d shows the sample AZ40T5 which shows a less porous structure that is supported with the physical properties that will be covered in the section below. When titania content is increased to 7 wt%, liquid phase and particle bloating can be observed in Fig. 4e and f.

3.4 The Physical Properties

Figure 5a shows the impact of firing temperatures on alumina–zinc oxide ceramic bodies' bulk density. Generally, an increase in the firing temperature from 1550 to 1650 °C results in an increase in the bulk density for AZ samples. For example, the bulk density of sample AZ0 increases from 2.25 to 2.76 g/cm³ by increasing the firing temperature from 1550 to 1650 °C. Figure 5b shows the effect of the firing temperature on the bulk density of TiO_2–$ZnAl_2O_4$ spinel ceramic bodies. Increase the firing temperature results in an increase in the bulk density of AZT samples. For example, the bulk density of the sample AZ40T7 increases from 1.59 to 3.29 g/cm³ by increasing the firing temperature from 1450 to 1600 °C.

Figure 5c shows the effect of increasing ZnO wt% on the bulk density of alumina–zinc oxide ceramic bodies. Generally, the increase in the ZnO wt% results in a decrease of the bulk density. For example, at the firing temperature of 1650 °C, the bulk density decreases from
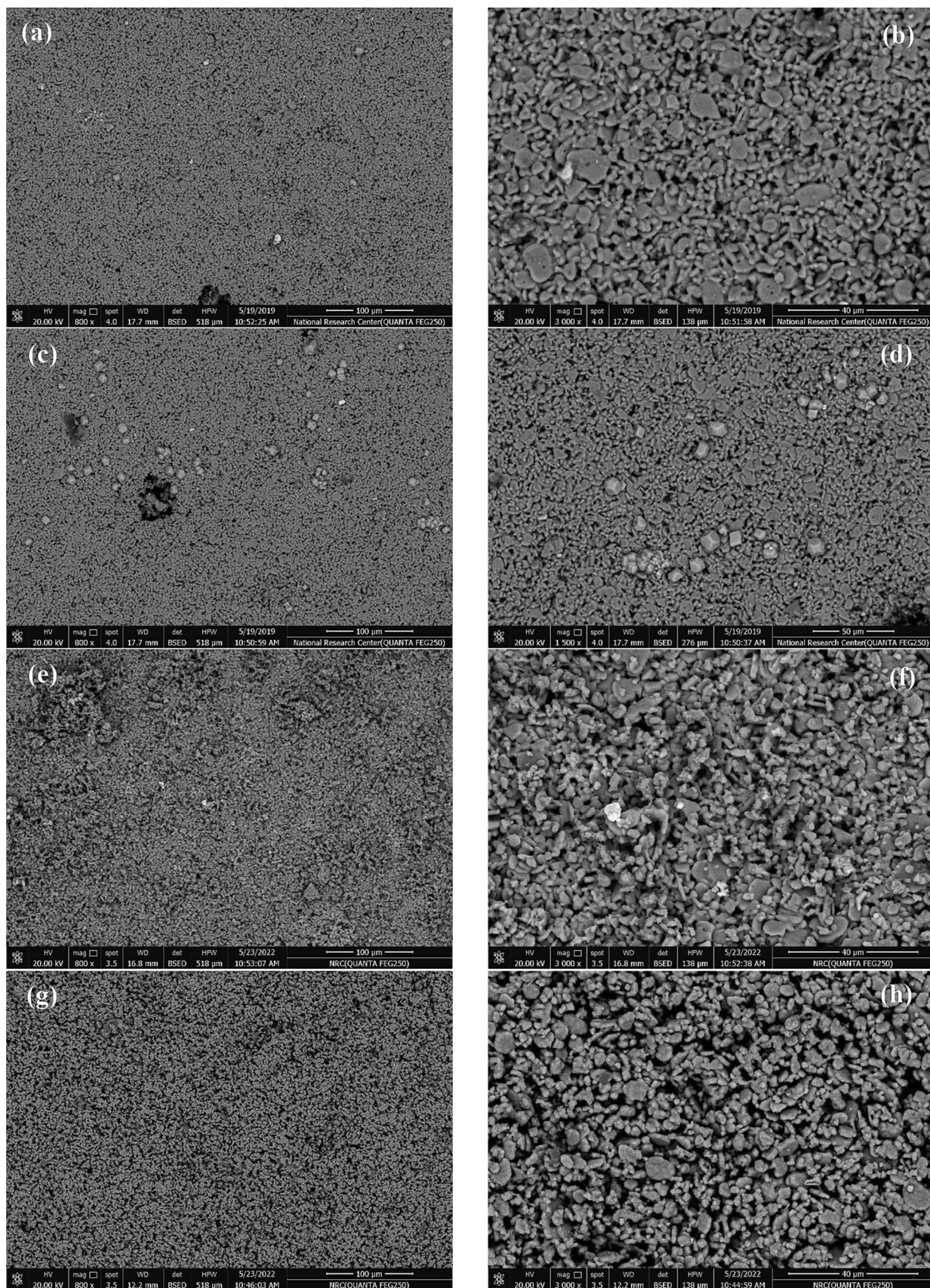
Fig. 3 SEM photos of alumina–zinc oxide samples: **a**, **b** for AZ0, **c**, **d** for AZ10, **e**, **f** for AZ20, **g**, **h** for AZ30, and **i–j** for AZ40
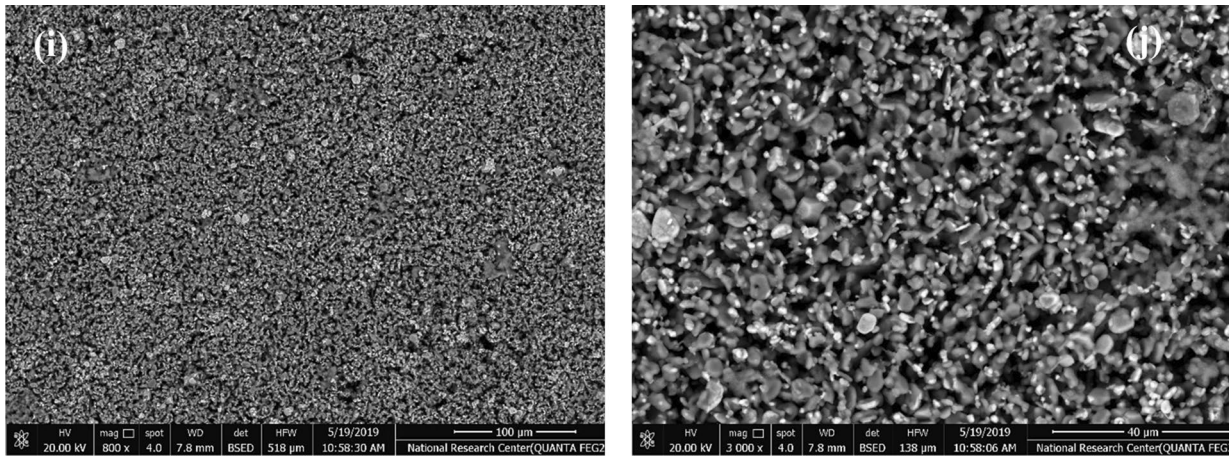
Fig. 3 (continued)

2.76 to 2.35 g/cm^3, 2.11 g/cm^3, 1.85 g/cm^3, and 1.72 g/cm^3 in AZ0, AZ10, AZ20, AZ30, and AZ40; respectively. According to the XRD results, the sample AZ40 is made up of pure gahnite which has a theoretical density of ~ 4.58 g/cm^3, while the bulk density of this sample is 1.72 g/cm^3. This indicates the success of DCC in the fabrication of high porous zinc aluminate spinel [47].

On the other hand, the apparent porosity of AZ samples fired at 1650 °C increases from 30.19 to 32.90%, 46.44%, 58.69%, and 59.10% in samples AZ0, AZ10, AZ20, AZ30 and AZ40; respectively, as shown in Fig. 5d. As has been discussed in the XRD and microscopy results, the addition of ZnO hinders grain growth which indeed leaves pores. It has been reported that gahnite formation will leave pores and making it hard to achieve 100% density [51]. Alam et al. reported that zinc aluminate is formed when zinc oxide is incorporated with alumina and is accompanied with larger expansion [52].

Apart from the previously mentioned factors, the high porosity of the final product results from the utilization of a one-stage sintering process. During the initial heating stage up to 600 °C, there is a carbonization process occurring within the organic matter. Some of the organic components, including ACT, urea, and urease, react with oxygen in the air, leading to the formation of pores. Another portion of the organic matter, which remains shielded from direct contact with air, undergoes carbonization. Consequently, it continues to generate uniform pores in the subsequent sintering process at the elevated temperature of sintering leading to the formation of gahnite, forming pores that exhibit greater uniformity compared to those resulting from the sintering of organic matter alone. As a result, the sintering process contributes to the reduction in bulk density within the range of 2.35–1.72 g/cm^3, alongside significant thermal expansion [53]. The DCC method

succeeded in creating spinel bodies of zinc aluminate with an apparent porosity reaching 60%.

Comparing this product to porous alumina prepared through the gel-casting process [53], which involved constructing interlocked plate-like alumina structures using AlF$_3$ and silica particles as starting materials and single-step firing in the temperature range of 1100 to 1500 °C, it's evident that this work exhibits favorable physical properties. In the gel-casting study, apparent porosity ranged from 82 to 76%, with bulk density between 0.53 and 0.66 g/cm^3.

Additionally, when compared to the work of An-Nan Chen et al., who produced porous alumina ceramics from alumina fibers using a combination of direct coagulation casting (DCC) and 3D printing [54], it's notable that the ceramics in this study demonstrate superior physical characteristics. After sintering at 1450 °C, Chen's work yielded ceramics with around 57.8% porosity and a strength of approximately 24 MPa. In contrast, this current work, fired at 1650 °C, exhibits porosity ranging from 30 to 58% and strength between 27 and 50 MPa, as detailed in Sect. 3.6. These enhanced physical properties position this work favorably for a broader range of applications in porous ceramics.

Figure 5e the effect of increasing TiO$_2$ wt% on the bulk density of TiO$_2$–ZnAl$_2$O$_4$ spinel ceramic bodies. The addition of 2 wt% TiO$_2$ results in the increase in the bulk density to 2.84 g/cm^3 for sample AZ40T2 compared to 1.61 g/cm^3 for sample AZ40; respectively when firing at 1600 °C. Increasing TiO$_2$ to 5% results in a further increase in the bulk density to 3.49 g/cm^3. A further increase in TiO$_2$ to 7% results in a slight decrease of bulk density to 3.28 g/cm^3. The same trend is observed at different temperatures of firing i.e., 1450 °C, 1500 °C, and 1550 °C.

The apparent porosity of all samples is inversely proportional to the bulk density, as shown in Fig. 5f. At firing
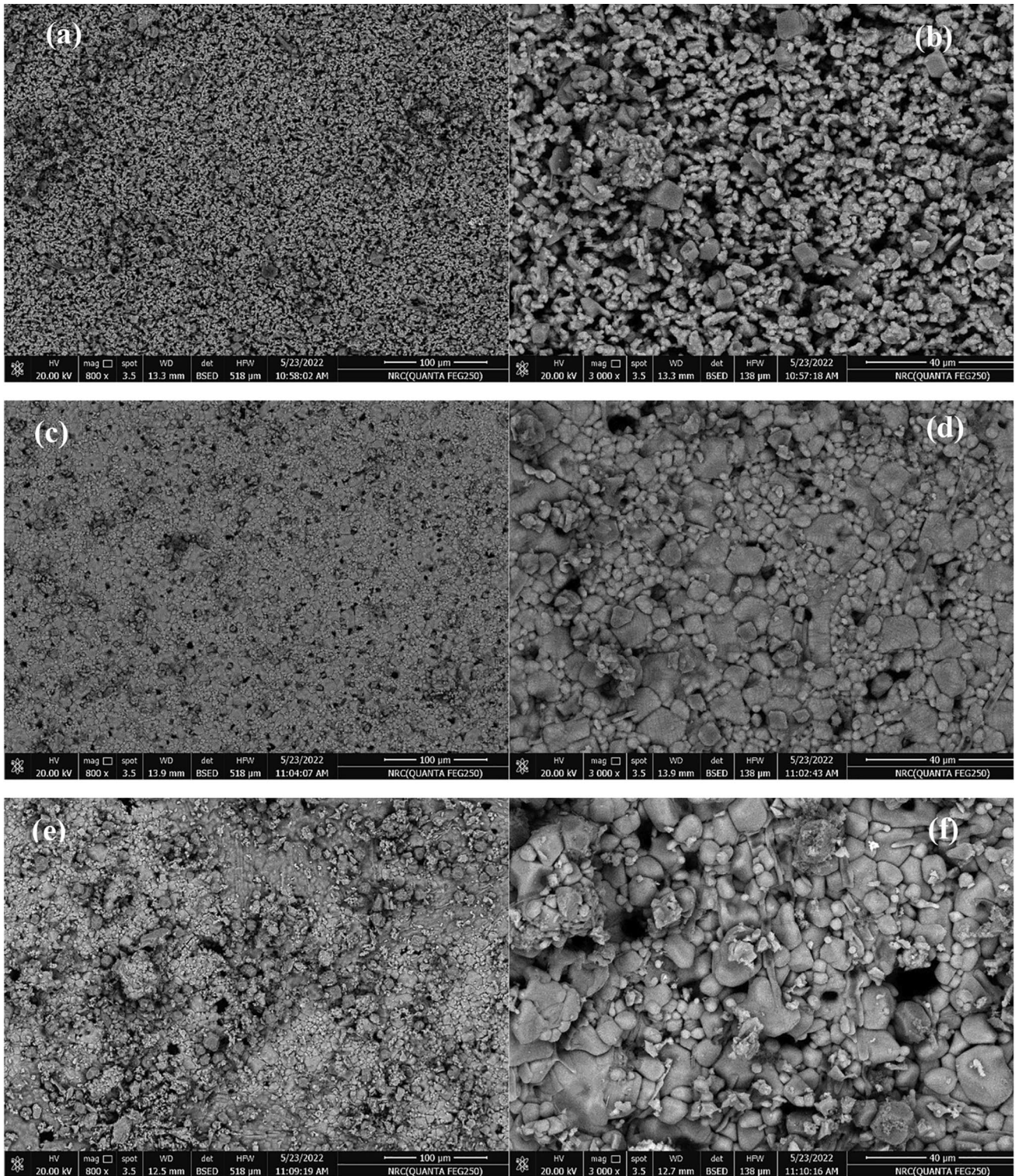
Fig. 4 SEM photos of TiO$_2$–zinc aluminate spinel ceramic bodied: **a**, **b** for AZ40T2, **c**, **d** for AZ40T5, and **e**, **f** for AZ40T7

temperature 1600 °C, increasing TiO$_2$ from 2 to 5 wt% resulted in a decrease in the apparent porosity from 46.85 to 5.63%. A further increase of TiO$_2$ to 7 wt% results in a decrease in apparent porosity to 25.63%. As can be seen

from SEM; Fig. 4; adding titania improves grain growth and resulted in an increase in bulk density and decreasing the porosity. This may be attributed to the formation of a liquid phase because of adding titania. It is worth mentioning that
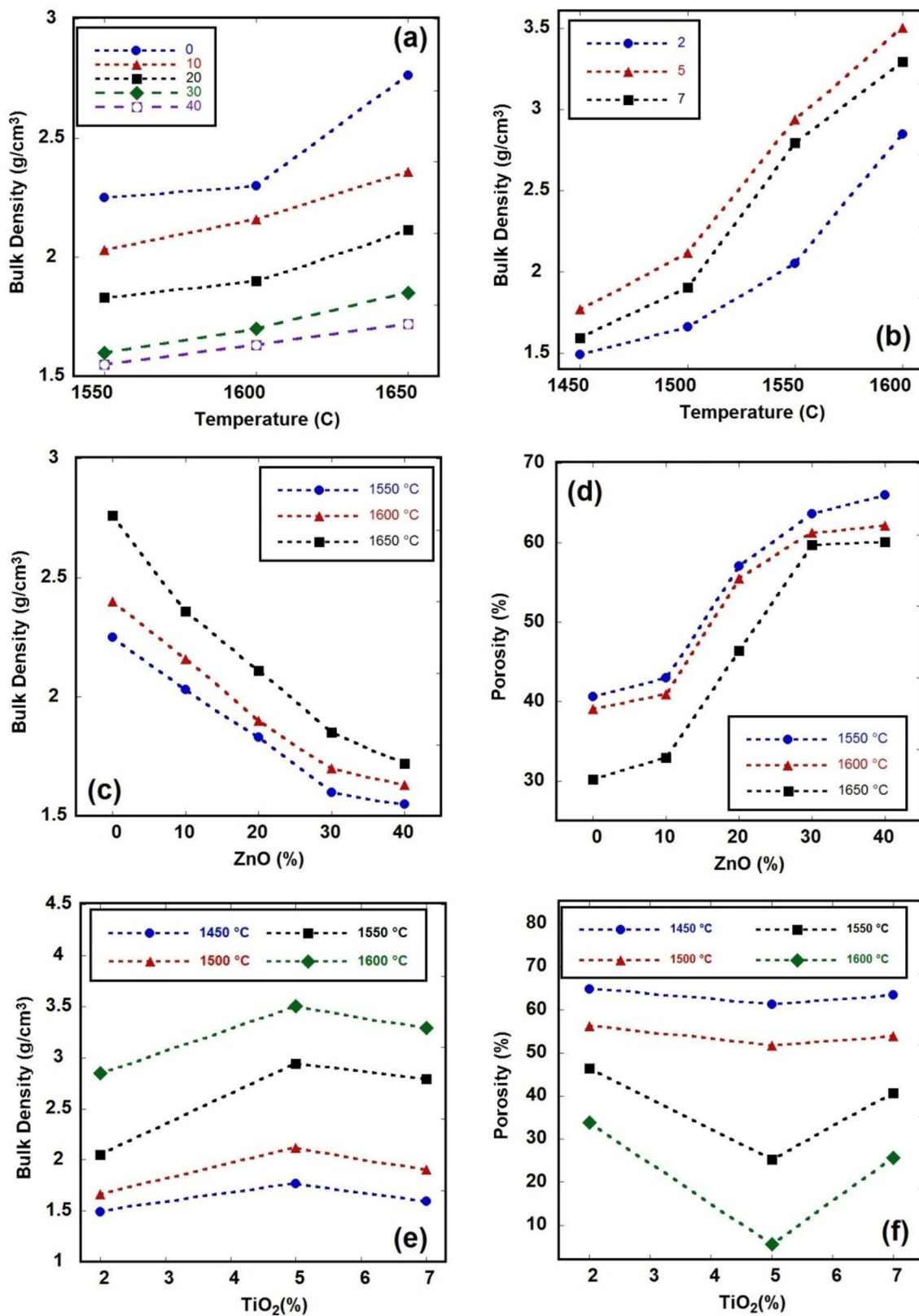
Fig. 5 The effect of firing temperature on the bulk density of **a** AZ samples, and **b** AZT samples; the effect of ZnO wt% on **c** the bulk density, and **d** the apparent porosity of AZ samples; the effect of TiO_2 wt% on the **e** bulk density, and **f** apparent porosity of AZT samples
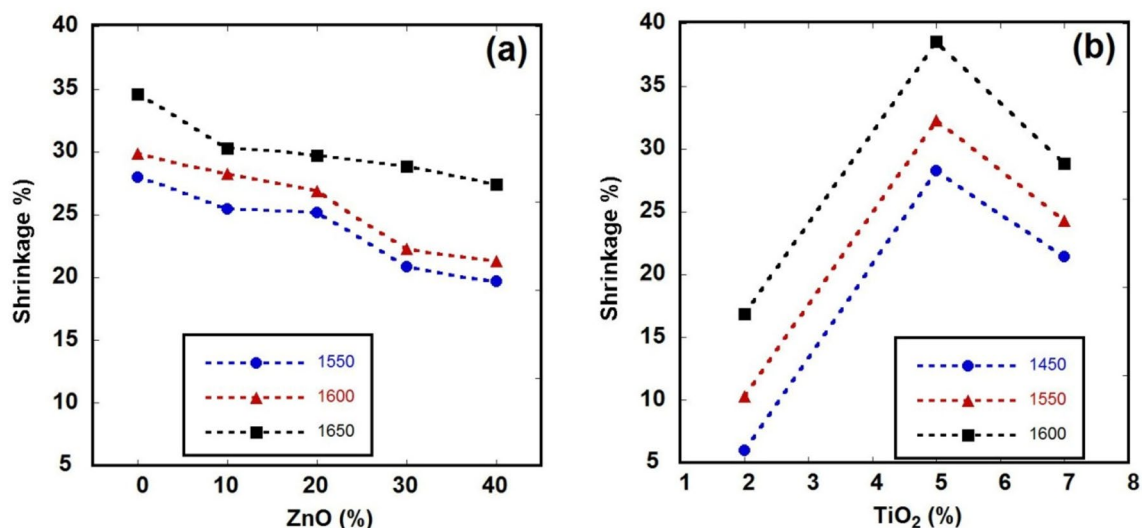
Fig. 6 Effect of the firing temperature and composition on the linear shrinkage of AZ samples (**a**) and AZT samples (**b**)

titania is used as a firing aid agent, which is reflected in better densification at lower temperatures. Because the melting point of TiO_2 (1830 °C) is lower than that of $ZnAl_2O_4$ (1980 °C), Ti^{4+} ions diffuse more easily [55]. Furthermore, the addition of transition metal oxides such as TiO_2, Cr_2O_3 or V_2O_5 helps the formation of double oxides such as mullite at lower temperatures with better grain growth [56].

The improved sinterability and the achievement of a single spinel phase formation in samples containing TiO_2, as opposed to those without TiO_2, can be attributed to the fact that TiO_2 introduces more interstitial and substitution defects in the solid solution that forms. Additionally, TiO_2 has the capacity to incorporate a greater number of ions into the structure, making it a more effective sintering aid [57].

Comparing this work with the study by Ghanbarnezhad et al., it's evident that this current research successfully produced ceramic samples with a higher bulk density of 3.49 g/cm^3 and a lower apparent porosity of 5.63%. In contrast, Ghanbarnezhad et al. achieved well-sintered samples with the addition of 4 wt% of TiO_2 on $MgAl_2O_4$ through solid-state reaction and sintering at 1600 °C, resulting in a bulk density of approximately 3.2 g/cm^3 and an apparent porosity of about 7% [57].

3.5 Linear Shrinkage

Figure 6a shows the linear shrinkage of DCC-shaped alumina–zinc oxide (AZ) ceramic bodies shaped by DCC and fired at 1550 °C, 1600 and 1650 °C. The linear shrinkage increases with increasing the firing temperature for each composition. For example, the linear shrinkage of sample AZ40 is about 19.7%, 21.3% and 27.4% at 1550 °C, 1600 and 1650 °C; respectively. Furthermore, the linear shrinkage

percentage increases with increasing fired temperature as the surface area is greatly reduced after firing. The linear shrinkage decreases when the weight% of ZnO increases. At 1650 °C, the increase in the ZnO wt%. from 0 to 40 wt% reduces the linear shrinkage from (34.6) to (27.4%). The results of linear shrinkage are consistent with the bulk density and the apparent porosity, Fig. 5c and d. As formerly stated in the physical properties, the increase in zinc oxide leads to the creation of gahnite and the reduction of the grain size, resulting in more porosity.

Figure 6b shows the effect of adding TiO_2 to the linear shrinkage of the AZ40 sample at different firing temperatures. The effect of increasing the firing temperature is the same as has been observed with AZ samples. Increase the firing temperature results in a higher linear shrinkage. The addition of titania results in a noticeable decrease in linear shrinkage compared to the AZT samples. For example, at a firing temperature of 1600 °C, the linear shrinkage for sample AZ40 is 21.3% which decreases to 16.9%. Adding more titania increases shrinkage to 38.6% followed by a decrease to 28.9% when titania increases to 7 wt%.

3.6 The Compressive Strength

The compressive strength of the alumina–zinc oxide (AZ) ceramic bodies fired at a temperature of 1650 °C is presented in Fig. 7a. The compressive strength drops from ~49.6 MPa to 27.2 when the ZnO wt% increases between zero and 40; respectively. It is founded that the rise in porosity may be responsible for the decrease in strength. The decrease in the mechanical strength coincides with the observed increase in the apparent porosity, shown in Fig. 5d, which increases from ~ 30–60%. Moreover, the microstructure of sample
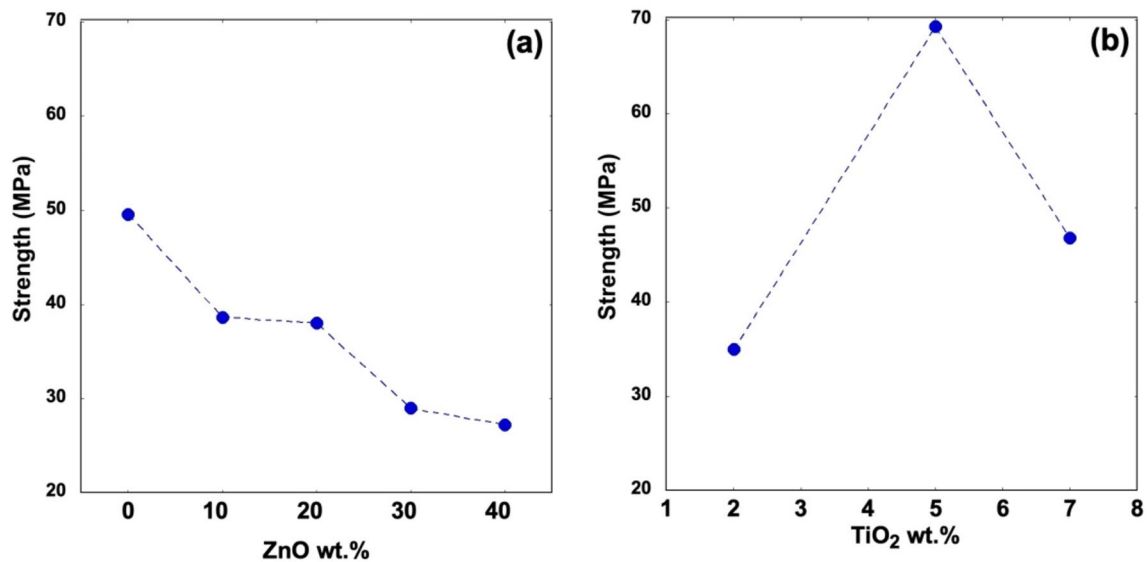
Fig. 7 Effect of composition on the compressive strength of **a** AZ samples and **b** AZT samples

AZ40 fired at 1650 °C, shown in Fig. 3i–j, shows the porosity of the sample.

The compressive strength of the TiO$_2$–zinc aluminate bodies fired at a temperature of 1600 °C is presented in Fig. 7b. The compressive strength increases from approximately 27.2 MPa for sample AZ40 to 35 MPa for sample AZ40T2; respectively. With increasing TiO$_2$ wt% to 5, the compressive strength increases to 69.2 MPa. The further increase in TiO$_2$ wt% to 7 results in a slight decrease of compressive strength to 46.8 MPa.

It has been demonstrated that increasing the compressive strength may is related to the decrease in porosity. The increase in compressive strength is coincides with the reduction of apparent porosity, shown in Fig. 5f. Furthermore, the microstructure of the AZ40T2, AZ40T5 and AZ40T7 sintered at 1600 °C in Fig. 3 show the behavior of the porosity of AZT samples.

Enhancing mechanical strength primarily involves reducing porosity, increasing crystallinity, and raising the density of ceramics. The presence of numerous pores within ceramics can impede the transfer and distribution of loads within the system (comprising crystals and residual glass phases), making them more susceptible to fracture. Moreover, maintaining lower porosity is crucial for preventing potential defects and flaws, including foreign particles that can serve as triggers for microcracks. Furthermore, dense, low-porosity ceramics are better equipped to withstand applied loads during compressive strength testing [58].

In comparison to the work of Wen Yan et al., it is evident that the optimized products in this study, involving the addition of 1.5% TiO$_2$ to porous spinel derived from magnesite and Al(OH)$_3$, sintered at 1600 °C, exhibit favorable characteristics. These products feature high apparent porosity (53.0%), a small average pore size (5.95 μm), and a compressive strength of 21.2 MPa. Consequently, this current research is well-suited for the preparation of ceramic bodies with superior strength when compared to the study by Wen Yan et al. [59].

3.7 Magnetic Properties

Magnetic momentum against magnetic field of the samples AZ and AZT are shown in Fig. 8. Most AZ samples show " S-type" magnetic curve which may be attributed to a mixed magnetic behavior. It is reported that alumina has a paramagnetic behavior and zinc oxide has a diamagnetic behavior due to the absence of unpaired 'd' electrons [60]. Figure 8b of sample AZ10 shows a butterfly-shape hysteresis which is attributed to a phonon bottle-neck effect [61]. Further increase of zinc oxide in samples AZ20 and AZ30 results in the disappear of butterfly shape. While sample AZ40 have a similar shape of AZ0. This may be attributed to the existence of defects, like interstitial oxygen and zinc vacancies, in the host lattice [62, 63]. Adding titania in AZ40T2 and AZ40T5 samples result in a more diamagnetic behavior and retards the magnetic behavior of the samples compared to AZ40 samples. This may be explained by a lot of Ti ions remain uncoupled.

in ZnAl$_2$O$_4$ structure and do not contribute to the magnetic behaviors. While sample AZ40T7 shows a "S-type" magnetic curve again. Thus, the magnetic behaviors for these samples depend on the TiO$_2$ concentrations. Thus, the magnetization of these samples is due to the incorporation of Ti^{4+} ions into the Zn^{2+} sites and the exchange-couple
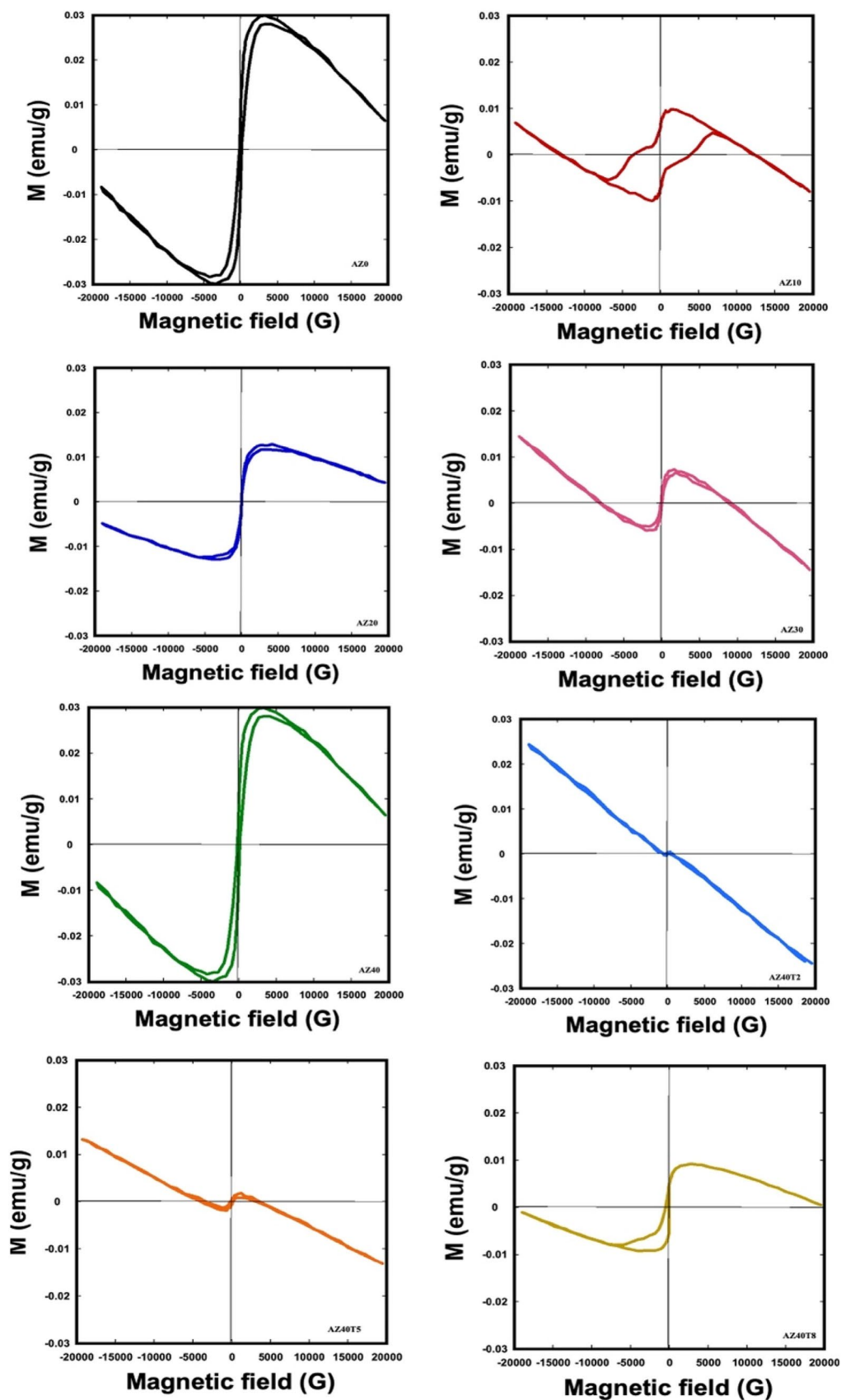
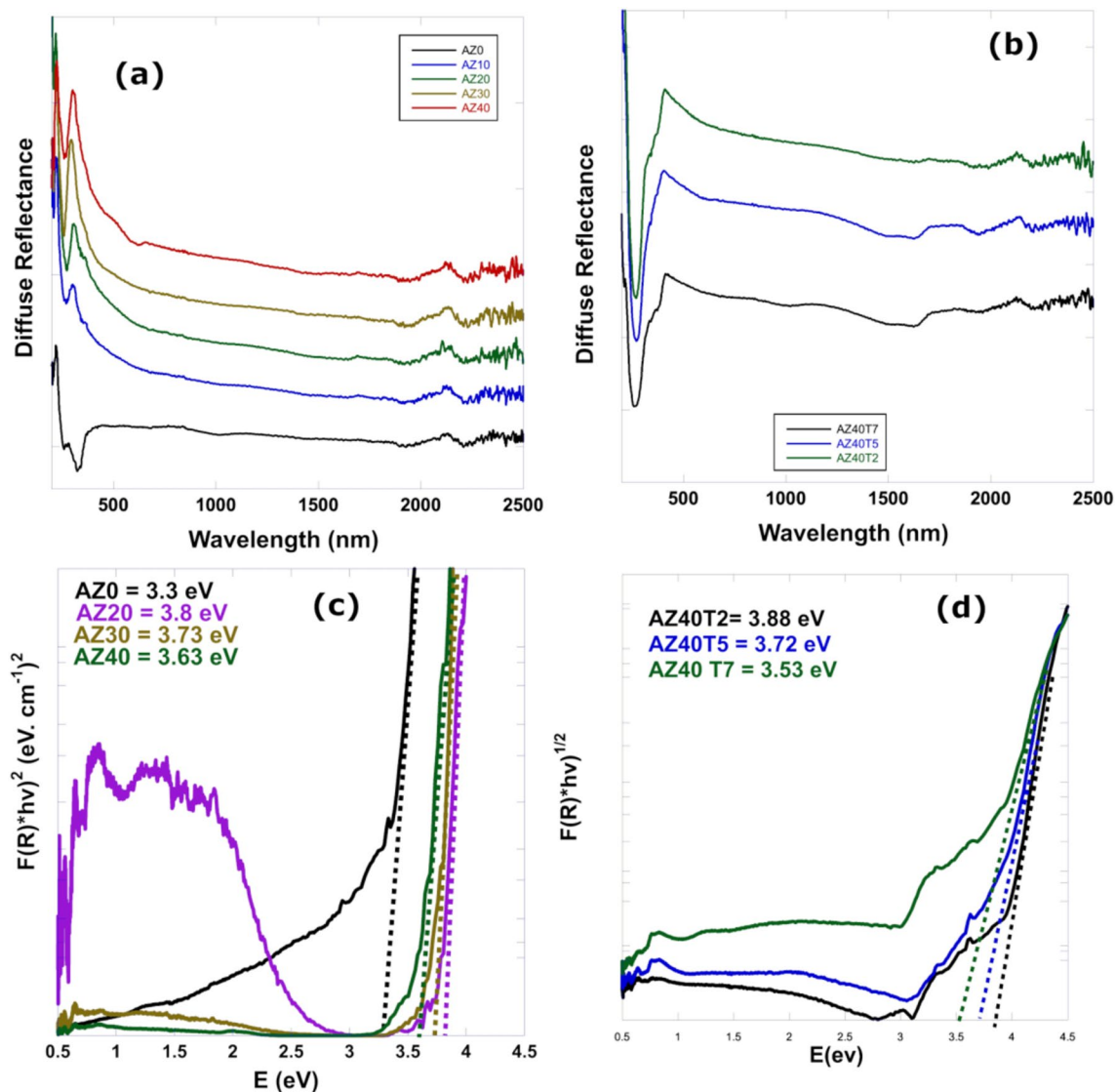**Fig. 8** Magnetic diagrams of AZ and AZT samples

Fig. 9 Diffuse reflection spectra of **a** AZ samples and **b** AZT samples, and the plot of (F (R)*hν)^2 against the photon energy (hν) of **c** AZ samples and **d** AZT samples

interaction between Ti^{4+} ions and Zn^{2+} ions [62, 64]. Zhang et al. prepared zinc aluminate by the hydrothermal method and found that undoped zinc aluminate crystals showed magnetism and when doped with Mn the magnetism disappear [2]. Anand et al. prepared zinc aluminate with microwave combustion and found that undoped zinc aluminate shows diamagnetic properties which changes to super paramagnetic properties when doped with cobalt [3].

3.8 Optical Diffused Reflection Spectra

Figure 9a and b shows the diffuse reflection spectra of AZ and AZT samples, respectively between 200 and 2500 nm in wave length. The reflectance peak was observed at 222 nm, 300 nm, 305 nm, 294 nm, and 298 nm for samples AZ0,

AZ10, AZ20, AZ30, and AZ40; respectively. This values suggests the potential of its application in anti-reflection coating [65]. After the addition of titania, the reflectance peak was observed at higher wavelength 400–420 nm due to presence of titanium ion [66]. The direct band gap was calculated according to Kubelka and Munk by drawing (F (R)*hν)^2 on the y-axis against hν on the x-axis as shown in Fig. 9c and d for AZ samples and AZT samples, respectively. The optical band gap of pure alumina, zinc oxide and titania are 2.8–4.3 eV [67, 68], 2.95–3.3 eV [69, 70], and 3.37–3.53 eV [71, 72], respectively. The calculated band gap for the samples AZ0, AZ20, AZ30 and AZ40 are 3.3, 3.8, 3.73, and 3.63 eV, The addition of zinc oxide (20%) results in the increase of the direct band gap while the further increase of zinc oxide results in a decrease of band gap

but it is still higher than the pure alumina. The addition of 2 wt% titania results in the increase of the band gap to 3.97 eV. The further increase of titania results in the decrease of band gap to 3.43 and 2.98 eV with 5 and 7 wt% of titania. Hussain et al. reported a band gap of 4.46 eV for $ZnAl_2O_4$ which was calcined at 900 °C [73]. It has been reported that zinc aluminate with optical band gap in 3.8–3.9 eV can be applied in ultraviolet photoelectronic devices, and photodetector [74]. It has been reported in the literature that the expose to high temperatures decline the values of band gap [72]. The values of the energy band gap could be impacted by contaminants and structural flaws such oxygen vacancies and interstitials. Consequently, decreasing Eg values could be caused by the aluminum and oxygen diffusion that resides in the spaces between the Al_2O_3 lattices [67]. Jamal et al. prepared pure gahnite powder by sol–gel and found its direct band gap of 3.84 eV [1]. Anand et al. reported that doping with cobalt concentration (0.1–0.5) resulted in narrowing the direct band gap from 4.98 to 2.89 eV. They referred this decrease due to the formation of subbands [3].

3.9 Antimicrobial Activity

All prepared composites show antibacterial activity against three microorganisms with different potentials as shown in Fig. 10. For *E. coli* bacteria, all eight composites show higher antibacterial activity than reference Gentamicin antibiotic. For *E. coli*, sample AZ40T7 shows the highest resistant with 20 mm inhibition zone (IZ) and the lowest IZ is 13 mm for sample AZ40 while reference has IZ of 12 mm. For. *S. aureus* bacteria, all samples show antibacterial behavior but only samples AZ0 and AZ40T5 are equivalent to reference antibiotic with IZ of 17 mm. For *B. cereus* bacteria, all samples show antibacterial behavior but with IZ less than reference antibiotic.

Numerous studies reported the mechanism of metal oxides in inhibiting the growth of microorganisms. Lakshmanan et al. reported that the positive ions are attracted to the negative cell wall and cause disturbance. This disturbance may cause a retard in the production of reactive oxygen species which is vital for the life of microorganisms [75]. The generation of superoxide ion (O_2^-), OOH* radicals, and hydrogen ions (H), which led to electron and hole interactions, was thought to be the cause of the bacterial inhibition. Due to this, proteins will become inactive, which will result in cell death [76]. Several studies report the antibacterial activity of ZnO and Al_2O_3 against *S. aureus* bacteria. Lakshmanan et al. measured the inhibition zone for

Cu-doped $ZnAl_2O_4$ (i.e. $Zn_{0.96}Cu_{0.04}Al_2O_4$) against *S. aureus* bacteria and it was 19 mm [75]. Brintha et al. prepared Al-doped ZnO and found that the inhibition zones against *E. coli* bacteria, *S. aureus* bacteria, and *C. albican* yeast are 9 mm, 8 mm, and 8 mm for undoped ZnO.

and inhibition zones increase to 13 mm, 12 mm, and 12 mm for Al-doped ZnO [77]. Comparing the previous results with the current work, showed that the AZ and AZT have high antimicrobial inhibition potentials.

Thus from the above, DCC method is able to prepare porous and structural ceramic bodies based on using ZnO and Al_2O_3 in absence or presence of TiO_2 to be used in various ceramic application. The utilization of alumina with zinc oxide in presence of small amount of TiO_2 can be used as ceramic substrates in electronic packages that are able to bear stress from screen printing, isostatic lamination pressing, cofiring, post-sintering machining, as well as from the heating and cooling of the device [78]. This sample can also be employed as a host matrix, ball milling media, optical coating for aerospace applications, or refractory material [79]. In case of the structure that containing alumina with 40 wt% of ZnO, the porous structure behavior was observed for this sample can be used as catalyst supports, gases filters, sensors, membrane reactors, and water treatment systems [80–84].

4 Conclusion

The DCC process successfully fills the notable research gap in forming porous zinc aluminate bodies when fired at high temperature. Adding zinc oxide to pure alumina results in the formation of a mixture of corundum and gahnite. Pure gahnite is achieved when the composition is 40 wt% zinc oxide and 60 wt% alumina and fired at 1650 °C. AZ40 sample has bulk density of 1.72 g/cm³, apparent porosity of 59% and compressive strength of 27.2 MPa. The addition of titania on the optimum selected AZ40 composition results in an improvement in the physical and mechanical properties at firing temperature 1600 °C. When TiO_2 is 5 wt%, the bulk density increases to 3.49 g/cm³, apparent porosity decreases to 5% and compressive strength reached 69.2 MPa. The samples show promising optical, magnetic and antibacterial activity. Thus, DCC can be used to prepare porous gahnite sample without TiO_2 addition and sintered gahnite sample after adding 5wt% TiO_2 to be applied in various ceramic applications.
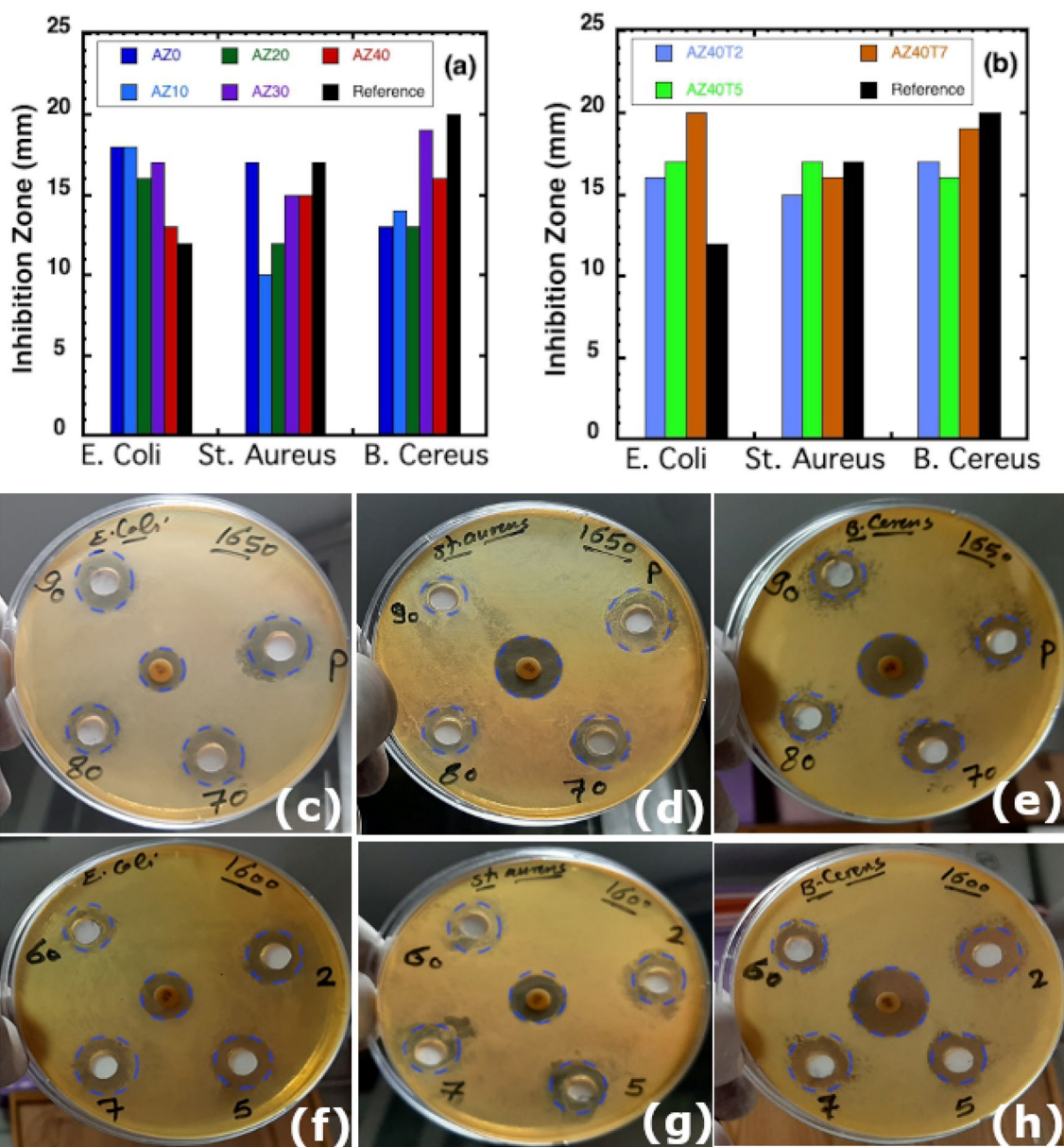
Fig. 10 Effect of **a** AZ composites and **b** AZT composites on the inhibition zones of different microorganisms, **c** image of inhibition zones of *E. coli* strains after incubation for 24 h under the effect of AZ composites, **d** image of inhibition zones of *S. aureus* strains after incubation for 24 h under the effect of AZ composites, **e** image of inhibition zones of *B. cereus* strains after incubation for 24 h under the effect of AZ composites, **f** image of inhibition zones of *E. coli* strains after incubation for 24 h under the effect of AZT composite, **g** image of inhibition zones of *S. aureus* strains after incubation for 24 h under the effect of AZT composites, and **h** image of inhibition zones of *B. cereus* strains after incubation for 24 h under the effect of AZT composites. (P=AZ0, 90=AZ10, 80=AZ20, 70=AZ30, 60=AZ40, 2=AZ40T2, 5=AZ40T5, and 7=AZ40T7)

Declarations

Competing interests The authors have no relevant financial or non-financial interests to disclose.

Ethical Approval Exempt from Ethical review; Approval for Exempt Review No.: EX010052023.

Consent to Participate All authors have agreed to participate in this research.

Consent for Publication The article was written by the named authors, who are all aware of its content and have given their permission for it to be published.

References

1. E.M.A. Jamal, D.S. Kumar, M.R. Anantharaman, On structural, optical and dielectric properties of zinc aluminate nanoparticles. Bull. Mater. Sci. **34**(2), 9 (2011)

2. D. Zhang, Y. Yin, Y. Liu, W. Chao, Y. Zhai, The photoluminescence and magnetic properties of $ZnAl_2O_4$:Mn nanocrystals. J. Phys. Chem. Solids **74**(8), 1131–1135 (2013). https://doi.org/10.1016/j.jpcs.2013.03.012

3. G.T. Anand, L.J. Kennedy, J.J. Vijaya, Microwave combustion synthesis, structural, optical and magnetic properties of $Zn_{1-x}Co_xAl_2O_4$ ($0 \leq x \leq 0.5$) spinel nanostructures. J. Alloys Compd. **581**, 558–566 (2013). https://doi.org/10.1016/j.jallcom.2013.07.081

4. S. Siragam, R.S. Dubey, L. Pappula, Investigation of structural, chemical, morphological and dielectric properties of sol–gel derived $ZnAl_2O_4$ nanoparticles. Mater. Today Proc. **45**, 2091–2095 (2021). https://doi.org/10.1016/j.matpr.2020.09.629

5. S. Siragam, R.S. Dubey, L. Pappula, G. Satheesh Babu, Synthesis and investigation of dielectric ceramic nanoparticles for microstrip patch antenna applications. Sci Rep **12**(1), 3929 (2022). https://doi.org/10.1038/s41598-022-07899-6

6. X. Xu, X. Xu, J. Wu, X. Lao, Fabrication and characterization of cordierite-based glass-ceramic adhesives for bonding solar heat transmission pipelines. Ceram. Int. **43**(1), 149–156 (2017). https://doi.org/10.1016/j.ceramint.2016.09.126

7. P. Pipattanaporn, P. Pansiri, P. Kumpeerakij, S. Yaemphutchong, P. Siri-apai, N. Suetrong, K. Chansaenpak, S. Singkammo, P. Kanjanaboos, Y. Hanlumyuang, S. Wannapaiboon, W. Wattanathana, Effect of triethanolamine chelating agent on crystallinities, phase purities, and optical properties of zinc aluminate spinel synthesized by thermal decomposition. Ceram. Int. **48**, 10 (2022)

8. S. Battiston, C. Rigo, E. Da Cruz Severo, M.A. Mazutti, R.C. Kuhn, A. Gündel, E.L. Foletto, Synthesis of zinc aluminate ($ZnAl_2O_4$) spinel and its application as photocatalyst. Mater. Res. **17**, 15 (2014)

9. A. Abd-Allah, A. Amin, A. Youssef, A. Ahmed, Fabrication of zinc aluminate ($ZnAl_2O_4$) nanoparticles from solid industrial wastes. Egytian J. Pure Appl. Sci. **60**(2), 13 (2022)

10. R. Venkatesh, L.S.R. Yadav, N. Dhananjaya, Rare earth activated bio synthesis of zinc aluminate for photocatalytic activity of dye. Mater. Today Proc. **49**, 4 (2021)

11. V. Baiju, D. Devadathan, G. Sajeevkumar, Photocatalytic degradation of toxic organic pollutants using zinc aluminate nanocomposite. Mater. Today Proc. **47**, 7 (2021)

12. M. Shaban, R. Hosny, A.M. Rabie, J.J. Shim, S.A. Ahmed, M.A. Betiha, N.A. Negm, Zinc aluminate nanoparticles: preparation, characterization and application as efficient and economic catalyst in transformation of waste cooking oil into biodiesel. J. Mol. Liq. **302**, 112377 (2020)

13. A.T.S.P. Putra, An improved method for high photocatalytic performance of $ZnAl_2O_4$ spinel derived from layered double hydroxide precursor. SN Appl. Sci. (2020). https://doi.org/10.1007/s42452-020-2682-7

14. L.E.C. Sotelo Martin, Al excess extends Hall-Petch relation in nanocrystalline zinc aluminate. J. Am. Ceram. Soc. **105**, 11 (2022)

15. A. Rahman, M.S. Charoo, R. Jayaganthan, Structural, optical and photocatalytic properties of zinc aluminate spinel nanoparticles. Mater. Technol. **30**, 9 (2015)

16. V. Baiju, D. Devadathan, P. Rejani, G. Sajeevkumar, R. Raveendran, Effect of annealing temperature in the purity of zinc aluminate synthesized by solution combustion method. AIP Conf. Proc. **2379**, 5 (2021)

17. S. Siragam, R.S. Dubey, L. Pappula, Investigation of structural, chemical, morphological and dielectric properties of sol–gel derived $ZnAl_2O_4$ nanoparticles. Mater. Today Proc. **45**, 5 (2021)

18. X.C. Wei, Synthesis and characterization of nanosized zinc aluminate spinel by sol–gel technique. Mater. Lett. **60**, 5 (2006)

19. M.A. Hessien, R.M. Khattab, M.A. Taha, H.E.H. Sadek, Fabrication of porous Al_2O_3–MgO–TiO_2 ceramic monoliths by the combination of nanoemulsion templating and temperature-induced forming. J. Eur. Ceram. Soc **41**(2), 1514–1523 (2021). https://doi.org/10.1016/j.jeurceramsoc.2020.09.056

20. H.E.H. Sadek, M.A. Hessien, Z.A. Abd El-Shakour, M.A. Taha, R.M. Khattab, The effect of sintering on the properties of magnesia-granite sludge ceramics shaped by temperature-induced forming. J. Mater. Res. Technol. **11**, 264–273 (2021). https://doi.org/10.1016/j.jmrt.2021.01.016

21. A.-N. Chen, J.-M. Wu, Y.-X. Liu, R.-Z. Liu, L.-J. Cheng, W.-L. Huo, Y.-S. Shi, C.-H. Li, Fabrication of porous fibrous alumina ceramics by direct coagulation casting combined with 3D printing. Ceram. Int. **44**(5), 4845–4852 (2018). https://doi.org/10.1016/j.ceramint.2017.12.073

22. M. Almeida, J.M. Vieira, Processing of ceramics by direct coagulation casting, in *Encyclopedia of materials: technical ceramics and glasses*. ed. by M. Pomeroy (Elsevier, Amsterdam, 2021), pp.154–161

23. R.M. Khattab, M.A. Hessien, N.I. El Abd, E. Abd, S.H. Rahim, H.E.H. Sadek, Porous alumina-felsite ceramic composites prepared by direct coagulation casting method: Felsite rock (central-eastern desert, Egypt). Ceram. Int. **46**(18), 28308–28315 (2020). https://doi.org/10.1016/j.ceramint.2020.07.334

24. T.C. Santos, S. d, D.R. Pinheiro, C.M.L. Costa, D.C. Estumano, N.F. Ribeiro, Synthesis and characterization of pigments based on copper-zinc aluminate ($CuxZn_{1-x}Al_2O_4$) by combustion. Ceram. Int. **46**(2), 2332–2343 (2020). https://doi.org/10.1016/j.ceramint.2019.09.224

25. C.S. Santos, T. Monte Almeida, A.C. Pinheiro, D.R. Leal Costa, C.M. Estumano, F. da Paixão, N. Ribeiro, Synthesis and

characterization of colourful aluminates based on nickel and zinc. J. Alloys Compd. (2020). https://doi.org/10.1016/j.jallcom.2019.152477

26. A.V. Belyaev, M.I. Lelet, N.I. Kirillova, N.M. Khamaletdinova, M.S. Boldin, A.A. Murashov, S.S. Balabanov, Sol–gel synthesis and characterization of ZnAl$_2$O$_4$ powders for transparent ceramics. Ceram. Int. **45**(4), 4835–4839 (2019). https://doi.org/10.1016/j.ceramint.2018.11.179

27. J.-M. Wu, H. Xiao, M.-Y. Liu, Y. Chen, Y.-X. Ma, L.-J. Cheng, Y.-S. Shi, Study of 0.9Al$_2$O$_3$–0.1TiO$_2$ ceramics prepared by a novel DCC-HVCI method. J. Adv. Ceram. **7**(2), 152–159 (2018). https://doi.org/10.1007/s40145-018-0266-4

28. Q. Wang, K. Xue, P. Fu, F. Du, Z. Lin, Z. Chen, S. Wang, G. Wang, Tunable dielectric properties of porous ZnAl$_2$O$_4$ ceramics for wave-transmitting devices. J. Mater. Sci. Mater. Electron. **30**(7), 6475–6481 (2019). https://doi.org/10.1007/s10854-019-00952-7

29. A. Dra, K. Tanji, A. Arrahli, E.M. Iboustaten, El. A. Gaidoumi, A. Kherchafi, A. Chaouni Benabdallah, A. Kherbeche, Corrigendum to "valorization of Oued Sebou natural sediments (Fez-Morocco Area) as adsorbent of methylene blue dye: kinetic and thermodynamic study." Sci. World J. **2020**, 1–1 (2020). https://doi.org/10.1155/2020/4815767

30. K. Tanji, E.I. Mrabet, Y. Fahoul, I. Jellal, M. Benjelloun, M. Belghiti, M. El Hajam, Y. Naciri, E.A. Gaidoumi, B. El Bali et al., Epigrammatic progress on the photocatalytic properties of ZnO and TiO$_2$ based hydroxyapatite@photocatlyst toward organic molecules photodegradation: a review. J. Water Process. Eng. (2023). https://doi.org/10.1016/j.jwpe.2023.103682

31. T. Tangcharoen, J. Thienprasert, C. Kongmark, Photocatalytic performance of Fe-substituted ZnAl$_2$O$_4$ powders under sunlight irradiation on degradation of industrial dyes. Int. J. Appl. Ceram. Technol. **18**(4), 1125–1143 (2021). https://doi.org/10.1111/ijac.13765

32. P. Pipattanaporn, P. Pansiri, P. Kumpeerakij, S. Yaemphutchong, P. Siri-apai, N. Suetrong, K. Chansaenpak, S. Singkammo, P. Kanjanaboos, Y. Hanlumyuang et al., Effect of triethanolamine chelating agent on crystallinities, phase purities, and optical properties of zinc aluminate spinel synthesized by thermal decomposition. Ceram. Int. **48**(6), 8186–8195 (2022). https://doi.org/10.1016/j.ceramint.2021.12.021

33. E.L. Foletto, B.S. Simões, J.M. Bassaco, M.M. Pereira, L.S.F. Flores, Synthesis of ZnAl$_2$O$_4$ nanoparticles by different routes and the effect of its pore size on the photocatalytic process. Microporous Mesoporous Mater. **163**, 5 (2012)

34. Fabian M, E. A., Kostova N, Briančin J and Baláž P. Photocatalytic activity of nanocrystalline gahnite (ZnAl$_2$O$_4$) synthesized by ball milling. In: the 12th international multidisciplinary scientific geo conference, Bulgaria, 2012; pp 491–498.

35. L. Zhao, X.Y. Li, J. Zhao, Fabrication, characterization and photocatalytic capability of ZnAl$_2$O$_4$ nanosphere. Adv. Mater. Res. **518**, 736–739 (2012)

36. R. Huo, K.Y. Zhao, Z. Zhang, S. Xu, Enhanced photocatalytic performances of hierarchical ZnO/ZnAl$_2$O$_4$ microsphere derived from layered double hydroxide precursor spray-dried microsphere. J. Colloid Interface Sci. **407**, 4 (2013)

37. M.K.M.H. Beate Balzer, J. Ludwig, Gauckler. coagulation kinetics and mechanical behavior of wet alumina green bodies produced via DCC. J. Colloid Interface Sci. **216**, 8 (1999)

38. ASTM, *Standard test methods for apparent porosity, water absorption, apparent specific gravity, and bulk density of burned refractory brick and shapes by boiling water* (ASTM, West Conshohocken, 2015)

39. R.M. Khattab, M.M.S. Wahsh, N.M. Khalil, Ceramic compositions based on nano forsterite/nano magnesium aluminate spinel powders. Mater. Chem. Phys. **166**, 82–86 (2015). https://doi.org/10.1016/j.matchemphys.2015.09.030

40. J. Chen, Y. Huang, Z. Ding, X. Liang, H. Lu, E-test or agar dilution for metronidazole susceptibility testing of Helicobacter pylori: importance of the prevalence of metronidazole resistance. Front. Microbiol. **13**, 801537 (2022). https://doi.org/10.3389/fmicb.2022.801537

41. S. Hu, S. Liu, F. Ye, H.C. Chen, Aqueous tape casting and properties of cordierite based glass-ceramics. Phys. Chem. Glasses Eur. J. Glass Sci. Technol. Part B **58**(1), 28–32 (2017). https://doi.org/10.13036/17533562.58.1.096

42. E. Emad, A.A. Zaman, W. Sigmund, Temperature induced forming of zirconia from aqueous slurries: mechanism and rheology. J. Eur. Ceram. Soc. **22**(16), 8 (2002)

43. N. El-Mehalawy, M. Awaad, T. Eliyan, M.A. Abd-Allah, S.M. Naga, Electrical properties of ZnO/alumina nano composites for high voltage transmission line insulator. J. Mater. Sci. Mater. Electron. **29**(16), 13526–13533 (2018). https://doi.org/10.1007/s10854-018-9480-7

44. S. Huang, Z. Wei, X. Wu, J. Shi, Optical properties and theoretical study of Mn doped ZnAl$_2$O$_4$ nanoparticles with spinel structure. J. Alloys Compd. **825**, 154004 (2020). https://doi.org/10.1016/j.jallcom.2020.154004

45. M.J. Sánchez-Rivera, M.J. Orts, V. Pérez-Herranz, S. Mestre, Effect of type and amount of alumina as dopant over the densification and the electrical properties of zinc oxide ceramic electrodes. Boletín de la Sociedad Española de Cerámica y Vidrio **60**(1), 53–61 (2021). https://doi.org/10.1016/j.bsecv.2020.01.003

46. T. Sofia Nirmala, N. Iyandurai, S. Yuvaraj, M. Sundararajan, Effect of Cu^{2+} ions on structural, morphological, optical and magnetic behaviors of ZnAl$_2$O$_4$ spinel. Mater. Res. Express. **7**(4), 046104 (2020). https://doi.org/10.1088/2053-1591/ab7a7a

47. W. Lei, W.-Z. Lu, J.-H. Zhu, X.-H. Wang, Microwave dielectric properties of ZnAl$_2$O$_4$–TiO$_2$ spinel-based composites. Mater. Lett. **61**(19–20), 4066–4069 (2007). https://doi.org/10.1016/j.matlet.2007.01.017

48. K.P. Surendran, M.T.S.M.V. Manjusha, A low loss, dielectric substrate in ZnAl$_2$O$_4$–TiO$_2$ system for microelectronic applications. J. Appl. Phys. **98**, 5 (2005). https://doi.org/10.1063/1.2007873

49. X.L. Wen Yan, J. Chen, N. Li, Y. Wei, B. Han, Effect of TiO$_2$ addition on microstructure and strength of porous spinel (MgAl$_2$O$_4$) ceramics prepared from magnesite and Al(OH)$_3$. J. Alloys Compd. **618**, 5 (2015)

50. A. Ghosh, S.K. Das, J.R. Biswas, H.S. Tripathi, G. Banerjee, The effect of ZnO addition on the densification and properties of magnesium aluminate spinel. Ceram. Int. **26**, 4 (2000)

51. N.J. van der Laag, M.D. Snel, P.C.M.M. Magusin, G. de With, Structural, elastic, thermophysical and dielectric properties of zinc aluminate (ZnAl$_2$O$_4$). J. Eur. Ceram. Soc. **24**(8), 2417–2424 (2004). https://doi.org/10.1016/j.jeurceramsoc.2003.06.001

52. T. Alam, K.H.A.A. Mahmud, M.F. Hasan, S.A. Shahir, H.H. Masjuki, M.A. Kalam, A. Imran, H.M. Mobarak, Effect of magnesia on zinc oxide stabilized nano alumina ceramic powder in sintering process and its impact on mechanical properties. Procedia Eng. **68**, 723–729 (2013). https://doi.org/10.1016/j.proeng.2013.12.245

53. M.W. Xue Dong, A. Guo, Y. Zhang, S. Ren, G. Sui, Synthesis and properties of porous alumina ceramics with inter-locked plate-like structure through the tert-butyl alcohol-based gel-casting method. J. Alloys Compd. **694**, 9 (2017)

54. A.N. Chen, J.M. Wu, Y.X. Liu, R.Z. Liu, L.J. Cheng, W.L. Huo, Y.S. Shi, Fabrication of porous fibrous alumina ceramics by direct coagulation casting combined with 3D printing. Ceram. Int. **44**, 8 (2018)

55. W.-Z. Lu, W. Lei, J.-H. Zhu, F. Liang, Calcining temperature dependence of microwave dielectric properties of (1−x)ZnAl$_2$O$_4$–xTiO$_2$ (x = 0.21) ceramics. Jpn. J. Appl. Phys. **46**, L724–L726 (2007). https://doi.org/10.1143/jjap.46.L724. (**No. 29**))

56. A. Olanrewaju, A.K. Oluseyi, S.K. Das, The effect of MgO and Cr_2O_3 on mullite formation from Nigeria sourced kaolin-calcined alumina sintered compacts. IOP Conf. Series: Mater. Sci. Engi. (2019). https://doi.org/10.1088/1757-899x/509/1/012007

57. Ghanbarnezhad S, Nemati A, Bavand-Vandchali M, Naghizadeh R (2013) Effect of TiO_2 in spinel formation and reactive sintering of Magnesia-rich ceramics. Int. J. Eng. Adv. Technol. **2** (3): 85

58. A. Husniyah, H.M. Lutpi, T.K. Abdullah, Hamisah Ismail effect of ZnO on the structural, physio-mechanical properties and thermal shock resistance of $Li_2O–Al_2O_3–SiO_2$ glass-ceramics. Ceram. Int. **48**(6), 10 (2022)

59. W. Yan, X. Lin, J. Chen, N. Li, Y. Wei, B. Han, Effect of TiO_2 addition on microstructure and strength of porous spinel ($MgAl_2O_4$) ceramics prepared from magnesite and $Al(OH)_3$. J. Alloys Compd. **618**, 4 (2015)

60. S. Roy, M.P. Ghosh, S. Mukherjee, Introducing magnetic properties in Fe-doped ZnO nanoparticles. Appl. Phys. A **127**(6), 451 (2021)

61. M.A. Mahdy, S.H. Kenawy, I.K. El Zawawi, E.M.A. Hamzawy, G.T. El-Bassyouni, Optical and magnetic properties of wollastonite and its nanocomposite crystalline structure with hematite. Ceram. Int. **46**(5), 6581–6593 (2020). https://doi.org/10.1016/j.ceramint.2019.11.144

62. T.R. Gurugubelli, B. Babu, K. Yoo, Structural, optical, and magnetic properties of cobalt-doped $ZnAl_2O_4$ nanosheets prepared by hydrothermal synthesis. Energies **14**(10), 2869 (2021). https://doi.org/10.3390/en14102869

63. R. Siddheswaran, R.V. Mangalaraja, M.E. Gómez, R.E. Avila, C.E. Jeyanthi, Room temperature ferromagnetism in combustion synthesized nanocrystalline Co, Al co-doped ZnO. J. Alloys Compd. **581**, 4 (2013)

64. N.M. Basith, J.J. Vijaya, L.J. Kennedy, M. Bououdina, S. Jenefar, V. Kaviyarasan, Co-doped ZnO nanoparticles: structural, morphological, optical, magnetic and antibacterial studies. J. Mater. Sci. Technol. **30**(11), 10 (2014)

65. M.H. Eisa, M.G. Faraj, Optical properties of Al-doped with zinc oxide (AZO) thin films with PLD technique. Dig. J. Nanomater. Biostruct. **17**(3), 705–714 (2022). https://doi.org/10.15251/djnb.2022.173.705

66. P. Lopez-Iscoa, L.P.J. Massera, D. Janner, N.G. Boetti, D. Pugliese, S. Fiorilli, C. Novara, F. Giorgis, D. Milanese, Effect of the addition of Al_2O_3, TiO_2 and ZnO on the thermal, structural and luminescence properties of Er^{3+}-doped phosphate glasses. J. Noncryst. Solids **460**, 8 (2017)

67. Oleiwi, H. F. Al-Taay, H. F. Al-Ani, S. K. Y. Tahir, K. J. (2019) Structural and optical properties of Al_2O_3 nanocrystalline: effect of deposition time. In: The 7th International conference on applied science and technology (Icast 2019).

68. I. Costina, R. Franchy, Band gap of amorphous and well-ordered Al_2O_3 on Ni_3Al. Appl. Phys. Lett. (2001). https://doi.org/10.1063/1.1380403

69. C. Xia, Z. Qiao, L. Shen, X. Liu, Y. Cai, Y. Xu, J. Qiao, H. Wang, Semiconductor electrolyte for low-operating-temperature solid oxide fuel cell: Li-doped ZnO. Int. J. Hydrog. Energy **43**(28), 12825–12834 (2018). https://doi.org/10.1016/j.ijhydene.2018.04.121

70. V. Srikant, D.R. Clarke, On the optical band gap of zinc oxide. J. Appl. Phys. **83**(10), 5447–5451 (1998). https://doi.org/10.1063/1.367375

71. L. Mahoney, R.T. Koodali, Versatility of evaporation-induced self-assembly (EISA) method for preparation of mesoporous TiO_2 for energy and environmental applications. Materials (Basel) **7**(4), 2697–2746 (2014). https://doi.org/10.3390/ma7042697

72. M.P. Gonullu, H. Ates, The characteristic evolution of TiO_2/Al_2O_3 bilayer films produced by ALD: effect of substrate type and wide range annealing temperature. Superlattices Microstruct. **142**, 106529 (2020). https://doi.org/10.1016/j.spmi.2020.106529

73. T. Hussain, M. Junaid, S. Atiq, S.K. Abbas, S.M. Ramay, B.F. Alrayes, S. Naseem, Tunable dielectric behaviour and energy band gap range of $ZnAl_2O_4$ ceramics mediated by mg substitution. J. Alloys Compd. **724**, 940–950 (2017). https://doi.org/10.1016/j.jallcom.2017.07.104

74. M. Amghar, A. Bougoffa, A. Trabelsi, A. Oueslati, E. Dhahri, Optical and dielectric properties of silver-substituted $ZnAl_2O_4$ spinels synthesized using a sol–gel auto-combustion method. RSC Adv. **12**(31), 20348–20359 (2022). https://doi.org/10.1039/d2ra02555h

75. A. Lakshmanan, P. Surendran, S. SakthyPriya, K. Balakrishnan, T.A. Hegde, G. Vinitha, G. Ramalingam, B. Ravindran, S.W. Chang, M.S. Elshikh et al., Effect of fuel content on nonlinear optical and antibacterial activities of $Zn/Cu/Al_2O_4$ nanoparticles prepared by microwave-assisted combustion method. J. King Saud Univ. Sci. **32**(2), 1382–1389 (2020). https://doi.org/10.1016/j.jksus.2019.11.031

76. T. Tatarchuk, B. Al-Najar, M. Bououdina, M.A.A. Ahmed, Catalytic and photocatalytic properties of oxide spinels, in *Handbook of Ecomaterials* ed. by L. Martínez, O. Kharissova, B. Kharisov (Springer, Cham, 2019), pp. 1701–1750. https://doi.org/10.1007/978-3-319-68255-6_158

77. S. Gavrilets, J. Auerbach, van M. Vugt, Convergence to consensus in heterogeneous groups and the emergence of informal leadership. Sci. Rep. **6**, 29704 (2016). https://doi.org/10.1038/srep29704. From NLM Medline

78. S.B. Roshni, M.T. Sebastian, K.P. Surendran, Can zinc aluminate–titania composite be an alternative for alumina as microelectronic substrate. Sci. Rep. (2017). https://doi.org/10.1038/srep40839.2

79. A.A. Abd-Allah, A. Amin, A. Youssef, Y. Ahmed, Fabrication of zinc aluminate ($ZnAl_2O_4$) nanoparticles from solid industrial wastes. Egypt. J. Pure Appl. Sci. **60**(2), 13 (2022)

80. F. Rouabhia, A. Nemamcha, H. Moumeni, Elaboration and characterization of mullite anorthite-albite porous ceramics prepared from Algerian kaolin. Cerâmica **64**, 7 (2018)

81. J.T. Richardson, Y.P.D. Remue, Properties of ceramic foam catalyst supports: pressure drop. Appl. Catal. A **204**(1), 13 (2000). https://doi.org/10.1016/S0926-860X(00)00508-1

82. J. Li, H. Lin, J. Li, Factors that influence the flexural strength of SiC-based porous ceramics used for hot gas filter support. J. Eur. Ceram. Soc. **31**(5), 6 (2011). https://doi.org/10.1016/j.jeurceramsoc.2010.11.033

83. D.F. Anne Julbe, C. Guizard, Porous ceramic membranes for catalytic reactors—overview and new ideas. J. Membr. Sci. **181**(1), 16 (2001). https://doi.org/10.1016/S0376-7388(00)00375-6

84. M. Doaa, M.M.S. EL-Mekkawi, Removal of Pb^{2+} from water by using Na-Y zeolites prepared from egyptian kaolins collected from different sources. J. Environ. Chem. Eng. **2**(1), 8 (2014). https://doi.org/10.1016/j.jece.2013.11.014